High-Order Switching Surface in Boundary Control of Inverters

Julian Yat-Chung Chiu, *Student Member, IEEE*, Kelvin Ka-Sing Leung, *Member, IEEE*, and Henry Shu-Hung Chung, *Senior Member, IEEE*

***Abstract*—A high-order switching surface for boundary control of inverters is presented in this paper. The concept is based on using the natural response of the power stage to formulate a logarithmic function to approximate the ideal switching surface. With the proposed control method, the inverter exhibits better dynamic responses than the ones with the first-order or recently proposed second-order switching surfaces. It will also be shown that the first-order and second-order switching surfaces are the low-order approximations of high-order switching surface. As the high-order switching surface is close to the ideal switching surface, its high trajectory velocity along the switching surface makes the inverter state trajectory move toward the steady-state operating point in two switching actions under large-signal disturbances. The effects of the parametric variations on the output voltage and the large-signal characteristics of the inverter will be discussed. The proposed control method has been successfully applied to a 300-W, 110-V, 60-Hz, single-phase full-bridge inverter. The steady-state and large-signal dynamic behaviors of the inverter supplying to resistive, nonlinear inductive, and full-wave rectifier loads will be given.**

***Index Terms*—Boundary control, dc–ac converter, inverters, nonlinear control.**

I. Introduction

Apart from classical control theories [1]–[11], many recent works have focused on applying boundary-control-derived methods [12]–[23] to design controllers for switching inverters. Boundary control is a geometric based control approach suitable for switching converters [12], [13] featuring time-varying structures. Its advantage lies in its generality of controlling converter operation without differentiating startup, transient, and steady state periods, so it is possible to cope with large-signal disturbances in the input source and output load. The main objective of the boundary control method is to drive the converter to the steady state with the use of a switching surface to dictate the states of the switches. Typical switching surfaces used in switching converters are of first-order (σ^1), such as the sliding-mode control and hysteresis control [14]–[22]. Although those methods provide good large-signal response and stability, they exhibit the following constraints.

1) The control parameters, such as the slope of the switching surface in the sliding-mode control, cannot be obtained readily from the power stage component values. They are usually designed by considering the converter's particular behaviors, such as the startup transients or the steady-state behaviors [18].
2) The control method is only applicable for a particular operating mode, such as the continuous conduction mode in dc/dc converters. Steady-state errors will be introduced if the controller is applied to other operating modes, such as discontinuous conduction mode [23]. Thus, an additional control loop, such as an integral feedback, is required to compensate the steady-state error.
3) It requires several switching actions before settling to steady state after a large-signal disturbance. Some design strategies are optimized for a particular transient performance, such as the start up process [18], with one switching cycle. However, the designed control parameters cannot ensure similar performances in other large-signal disturbances.

Much research work extends the concept, such as using an adaptive approach in [24] and [25], in order to enhance the dynamics. Recently, the second-order switching surface (σ^2) has been proposed in [23], [26], and [27]. It approximates the ideal switching surface $(\sigma*)$ with a second-order function, in order to achieve the objective of settling switching transients in two switching actions. Since $\sigma*$ is load-dependent and σ^2 does not have the load information, the discrepancy between $\sigma*$ and σ^2 is dependent on the damping factor of the output circuit, or equivalently the value of the load impedance (Z) with respect to the output filter natural impedance (Z_C). Such discrepancy will increase if Z decreases and/or the converter state is far away from the operating point. Thus, this will make the converter require more switching actions to settle to the operating point during large-signal disturbances.

This paper gives a further enhancement on formulating the switching surface for inverters. A high-order switching surface (σ^N) is proposed. A logarithmic function is derived to approximate $\sigma*$. The inverter exhibits better dynamic response than the ones with σ^1 or σ^2. As the load characteristics is taken into account in the switching function, σ^N is close to $\sigma*$. The trajectory velocity along the switching surface is high that makes the trajectory ideally move toward the target operating point in two switching actions after a large-signal disturbance. The steady-state and large-signal characteristics have been studied. The proposed control method has been successfully applied to a 300-W, 110-V, 60-Hz full-bridge inverter. Experimental results

Manuscript received July 24, 2006; revised November 14, 2006. This work was supported by the Research Grants Council of the Hong Kong Special Administrative Region, China, under Project CityU 1129/05. Recommended for publication by Associate Editor José Pomilio.

The authors are with the Department of Electronic Engineering, City University of Hong Kong, Kowloon, Hong Kong, China (e-mail: eeshc@cityu.edu.hk).

Digital Object Identifier 10.1109/TPEL.2007.904209

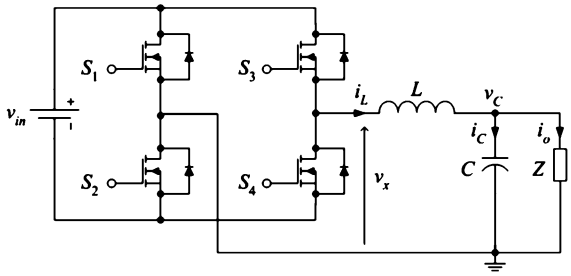

Fig. 1. Schematic diagram of a full-bridge inverter.

show that the total harmonic distortion of the output voltage is low with different load types, including resistive, nonlinear inductive, and full-wave rectifier loads. The system can revert to the steady state in two switching actions during large-signal disturbances in the input voltage, output load, and output reference.

II. Principles of Operation

Fig. 1 shows the schematic diagram of a full-bridge inverter, which can be described by the following state-space equations:

$$\dot{x} = A_0\, x + B_0\, v_{\text{in}} + (A_1 x + B_1 v_{\text{in}})q_1 + (A_2 x + B_2 v_{\text{in}})q_2 \quad (1)$$

where $x = [i_L v_C]$, i_L is the inductor current, v_C is the capacitor voltage and is equal to the load voltage, v_{in} is the input voltage, q_k represents the state of the switches, and A_k and B_k are constant matrices depending on the values of L, C, and the instantaneous ac load resistance R of the load Z. (S_2, S_3) are on if $\{q_1, q_2\} = \{1, 0\}$, and (S_1, S_4) are on if $\{q_1, q_2\} = \{0, 1\}$. Matrices A_0, B_0, A_1, B_1, A_2, and B_2 are defined as

$$A_0 = \begin{bmatrix} 0 & -1/L \\ 1/C & -1/RC \end{bmatrix}, \quad B_0 = \begin{bmatrix} 0 \\ 0 \end{bmatrix}, \quad A_1 = \begin{bmatrix} 0 & 0 \\ 0 & 0 \end{bmatrix}$$
$$B_1 = \begin{bmatrix} 1/L \\ 0 \end{bmatrix}, \quad A_2 = \begin{bmatrix} 0 & 0 \\ 0 & 0 \end{bmatrix}, \quad B_2 = \begin{bmatrix} -1/L \\ 0 \end{bmatrix}.$$

Fig. 2 shows families of trajectories that are obtained by solving (1) with different initial conditions. The inverter component values used are tabulated in Table I. The load is resistive and is given in Table II. The positive state trajectories are derived, when the inverter output voltage $v_x = v_{\text{in}}$ (i.e., with S_2 and S_3 on, and S_1 and S_4 off). The negative state trajectories are derived, when $v_x = -v_{\text{in}}$ (i.e., with S_2 and S_3 off, and S_1 and S_4 on). The tangential component of the trajectory velocity along the switching surface determines the rate at which successor points approach or recede from the operating point "O" [12]. Depending on the location of the initial state, for example the states "A" and "B" in Fig. 2, the ideal switching surface (σ^*) is along either the only positive state trajectory or negative state trajectory that passes through "O." A switching surface that has deviation from σ^* will make the inverter require more switching actions to slide along the surface or to swirl around "O" after a disturbance [12], [13], [18], [26], [27]. σ^2 has made a close approximation around the operating point [26], [27]. However, the settling time is still non-optimal under a large

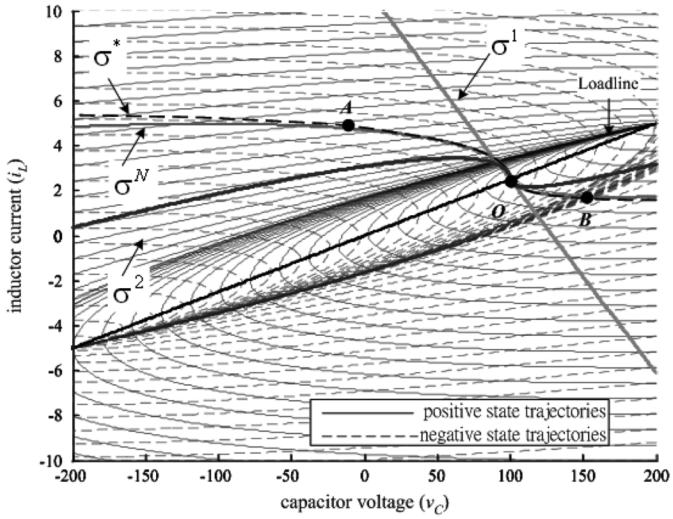

Fig. 2. Families of trajectories.

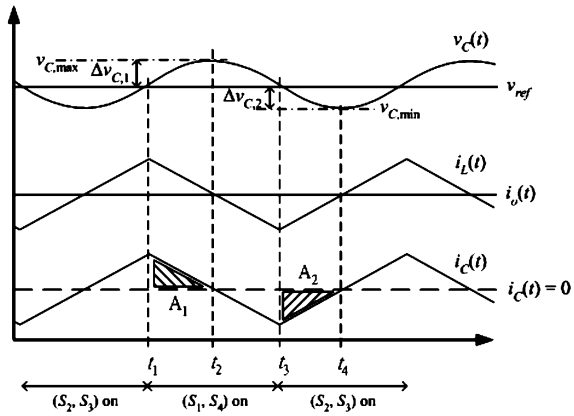

Fig. 3. Waveforms of v_C, i_L, i_o, and i_C.

disturbance that significantly deviates from the operating point. A high-order switching surface (σ^N) that can well approximate $\sigma*$ is derived in this paper. With the help of the key waveforms shown in Fig. 3, the switching criteria are given as follows.

A. Criteria for Switching on S_1 and S_4

As illustrated in Fig. 3, S_1 and S_4 are originally off and are switched on at the hypothesized time t_1. The objective is to determine t_1, so that $v_C(t_2) = v_{C,\max}$ and $i_C(t_2) = 0$ after S_1 and S_4 are on, and the inverter will follow the negative state trajectory (Fig. 2). Thus, $v_C(t_1), v_C(t_2), i_C(t_1)$, and $i_C(t_2)$ are known values while t_2 is an unknown value. The following assumptions have been made in deriving the switching criteria.

1) The parasitic resistances of the switches, inductor, and capacitor are neglected.
2) For the sake of simplicity in the analysis and implementation, the values of v_C and the inductor voltage v_L in the considered interval $[t_1, t_2]$ are assumed to be constant. Their values are approximated by averaging their values at t_1 and t_2. They are denoted by $\bar{V}_{C,1}$ and $\bar{V}_{L,1}$, respectively. The approximation is applicable because the switching frequency is much higher than the frequency of the reference

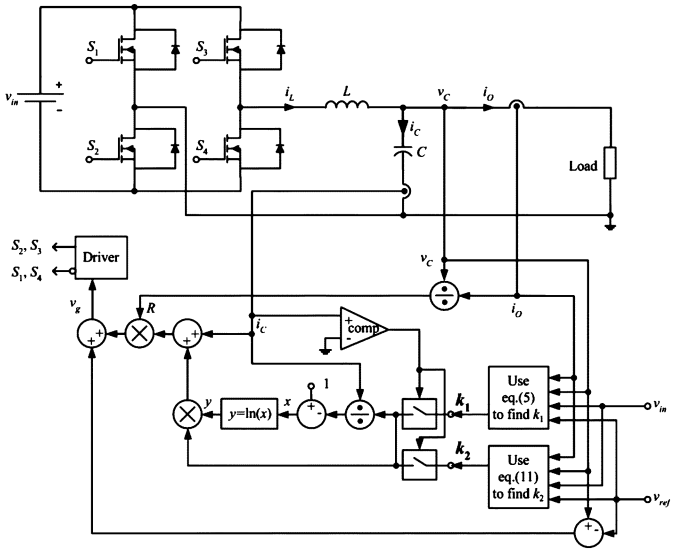

Fig. 4. Block diagram of the proposed high-order boundary controller.

voltage $v_{\rm ref}$ and the variation of $v_{\rm ref}$ (and thus v_C and v_L) within a switching cycle is small. Thus

$$v_C(t) = \bar{V}_{C,1} = \frac{v_C(t_1) + v_C(t_2)}{2} = \frac{v_C(t_1) + v_{C,\max}}{2} \tag{2}$$

and

$$v_L(t) = \bar{V}_{L,1} = -[v_{\rm in} + \bar{V}_{C,1})] = -\left[v_{\rm in} + \frac{v_C(t_1) + v_{C,\max}}{2}\right] \tag{3}$$

for $t_1 < t < t_2$.

By applying the Kirchoff's current law at the output node

$$\frac{di_C(t)}{dt} + \frac{v_L(t)}{L} + \frac{i_C(t)}{CR} = 0 \tag{4}$$

where i_o is the output current and $R = (\delta v_C)/(\delta i_o)$ is the instantaneous ac load resistance.

By multiplying (4) with $e^{(t/CR)}$ and solving it for i_C, it can be shown that

$$i_C(t) = [i_C(t_1) - k_1]e^{\frac{t_1 - t}{CR}} + k_1 \tag{5}$$

where $k_1 = (CR\bar{V}_{L,1})/(L)$.

Since $i_C(t_2) = 0$

$$t_2 = CR\ln\left[1 - \frac{i_C(t_1)}{k_1}\right] + t_1 \tag{6}$$

and

$$\Delta v_{C,1} = v_C(t_2) - v_C(t_1) = v_{C,\max} - v_C(t_1) = \frac{1}{C}\int_{t_1}^{t_2} i_C(t)dt. \tag{7}$$

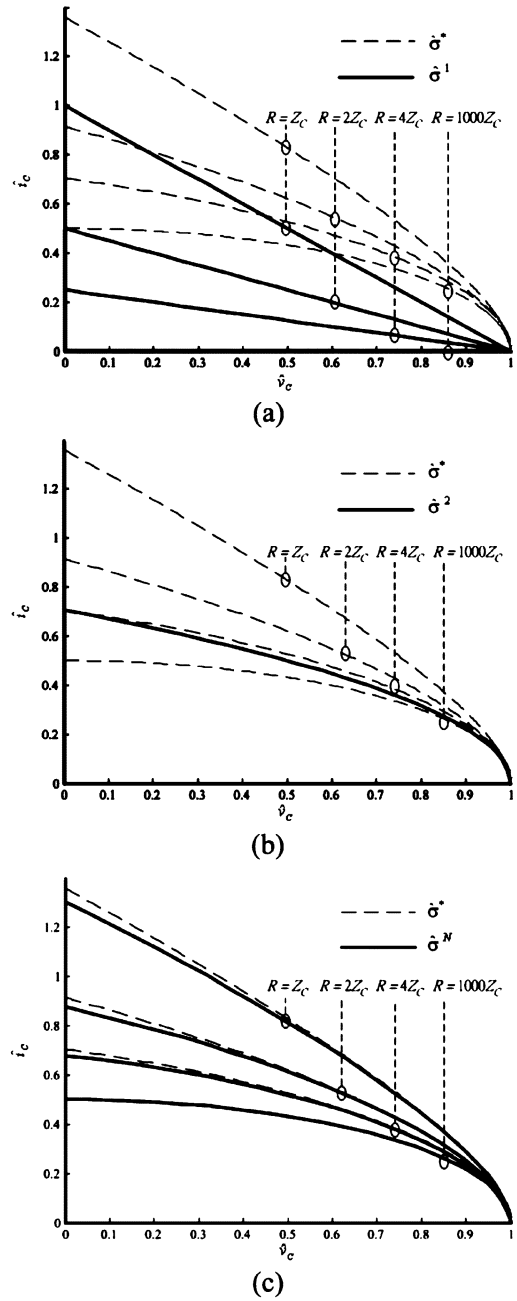

Fig. 5. Comparison of various normalized switching surfaces.

By solving (7) with (5) and (6), the criteria for switching S_1 and S_4 on and S_2 and S_3 off are

$$v_C(t_1) \geqslant v_{C,\max} - R\left[i_C(t_1) + k_1\ln\left(1 - \frac{i_C(t_1)}{k_1}\right)\right] \quad \text{and} \quad i_C(t_1) > 0. \tag{8}$$

B. Criteria for Switching on S_2 and S_3

As illustrated in Fig. 3, S_2 and S_3 are originally off and are switched on at the hypothesized time t_3. The objective is to determine t_3, so that $v_C(t_4) = v_{C,\min}$ and $i_C(t_4) = 0$ after S_2

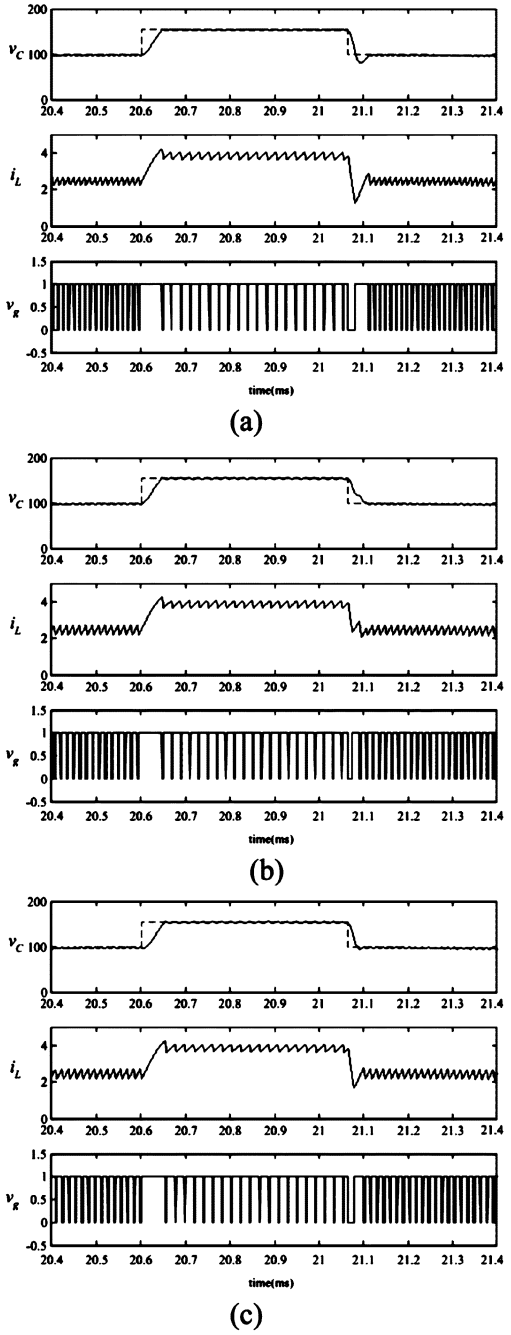

Fig. 6. Simulated time-domain waveforms of the inverter various switching surfaces under large-signal reference changes. (a) σ^1, (b) σ^2, and (c) σ^N.

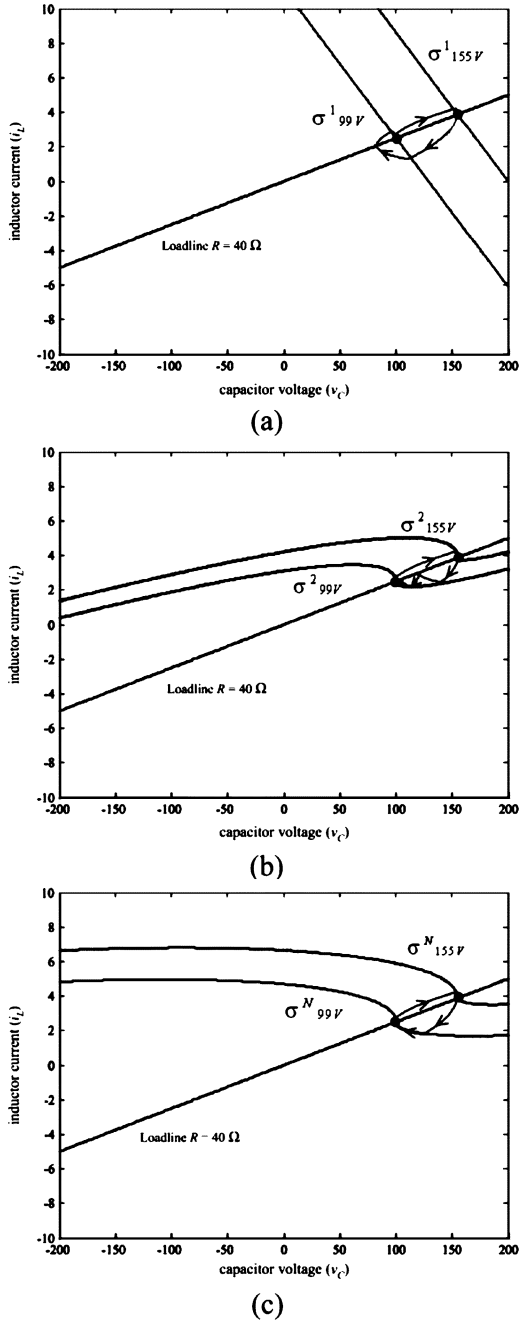

Fig. 7. Simulated state-space trajectories of the inverter various switching surfaces under large-signal reference changes. (a) σ^1, (b) σ^2, and (c) σ^N.

and S_3 are on, and the inverter will follow the positive state trajectory (Fig. 2). Thus, $v_C(t_3), v_C(t_4), i_C(t_3)$, and $i_C(t_4)$ are known values while t_4 is an unknown value. Similar to Section II-A, the following assumptions have been made in deriving the switching criteria.

1) The parasitic resistances of the switches, inductor, and capacitor are neglected.
2) For the sake of simplicity in the analysis and implementation, the values of v_C and the inductor voltage v_L in the considered interval $[t_3, t_4]$ are assumed to be constant. Their values are approximated by averaging their values at t_3 and t_4. They are denoted by $\bar{V}_{C,2}$ and $\bar{V}_{L,2}$, respectively. That is

$$v_C(t) = \bar{V}_{C,2} = \frac{v_C(t_3) + v_C(t_4)}{2} = \frac{v_C(t_3) + v_{C,\min}}{2} \quad \text{and} \tag{9}$$

$$v_L(t) = \bar{V}_{L,2} = v_{\text{in}} - \bar{V}_{C,2} = v_{\text{in}} - \frac{v_C(t_3) + v_{C,\min}}{2} \tag{10}$$

for $t_3 < t < t_4$.

TABLE I
COMPONENT USED IN THE SIMULATION AND PROTOTYPE

Parameter	Value
v_{in}	200 V
L	2mH
C	320nF

TABLE II
LOAD SPECIFICATION OF THE PROTOTYPE

Load (Z)	Value
Resistive	40Ω
Nonlinear Inductive	23mH + 40Ω
Full-wave rectifier load	264μF + 240Ω

TABLE III
COMPARISON OF THE SETTLING TIMES WITH DIFFERENT SWITCHING SURFACES

Switching surface	Settling time (μs)	
	From 70Vrms to 110Vrms	From 110Vrms to 70Vrms
σ^1	48.8	46.9
σ^2	42.7	46.9
σ^N	21.9	46.9

Again, by using (4) and similar technique for calculating (5), it can be shown that

$$i_C(t) = [i_C(t_3) - k_2]e^{\frac{t_3 - t}{CR}} + k_2 \tag{11}$$

where $k_2 = (CR\bar{V}_{L,2})/(L)$.

Since $i_C(t_4) = 0$

$$t_4 = CR\ln\left[1 - \frac{i_C(t_3)}{k_2}\right] + t_3 \tag{12}$$

and

$$\Delta v_{C,2} = v_C(t_4) - v_C(t_3) = v_{C,\min} - v_C(t_3) = \frac{1}{C}\int_{t_3}^{t_4} i_C(t)dt. \tag{13}$$

By solving (13) with (11) and (12), the criteria for switching S_2 and S_3 on, and S_1 and S_4 off are

$$v_C(t_3) \leqslant v_{C,\min} - R\left[i_C(t_3) + k_2\ln\left(1 - \frac{i_C(t_3)}{k_2}\right)\right] \quad \text{and} \quad i_C(t_3) < 0. \tag{14}$$

Fig. 3 shows the waveforms of the inverter with hysteresis bands added, in order to avoid frequency chattering. However,

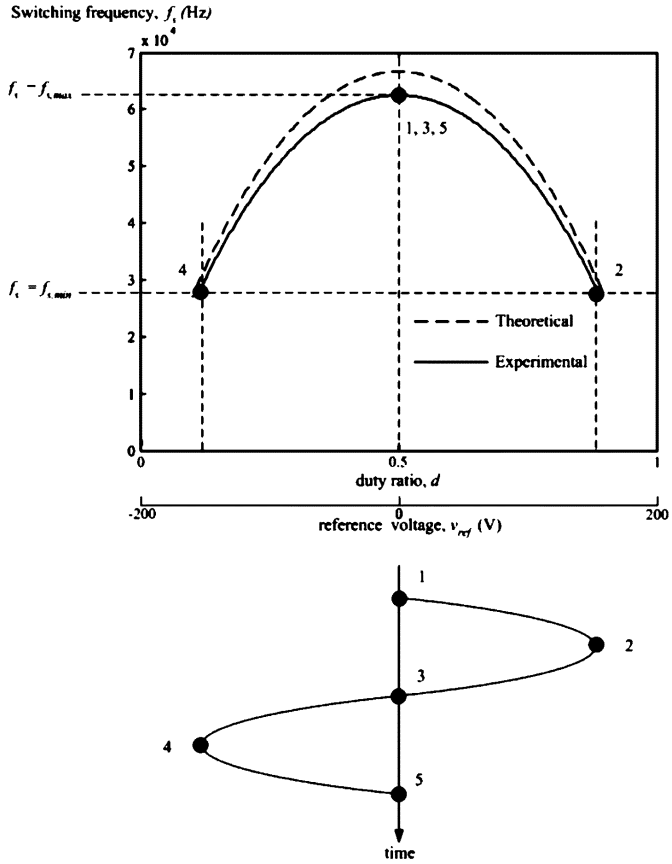

Fig. 8. Relationships between f_s and $v_{\rm ref}$.

for the sake of simplicity in design and analysis, the hysteresis band is ignored in the calculations. Thus, by combining (8) and (14) and putting $v_{C,\min} = v_{C,\max} = v_{\rm ref}$, the following switching surface σ^N is defined

$$\sigma^N(i_L, v_C) = \begin{cases} R\left[i_C + k_1\ln\left(1 - \frac{i_C}{k_1}\right)\right] + (v_C - v_{\rm ref}) \\ R\left[i_C + k_2\ln\left(1 - \frac{i_C}{k_2}\right)\right] + (v_C - v_{\rm ref}) \end{cases} \tag{15}$$

where $i_C = i_L - (v_C)/(R)$.

The equation can be written into a general form of

$$\sigma^N(i_L, v_C) = R\left[i_C + c_1\ln\left(1 - \frac{i_C}{c_1}\right)\right] + (v_C - v_{\rm ref}) \tag{16}$$

where $c_1 = (k_1)/(2)[1 + \mathrm{sgn}(i_C)] + (k_2)/(2)[1 - \mathrm{sgn}(i_C)]$ and $i_C = i_L - (v_C)/(R)$.

Fig. 2 shows σ^N in the state plane. Fig. 4 shows the block diagram of the proposed high-order boundary controller.

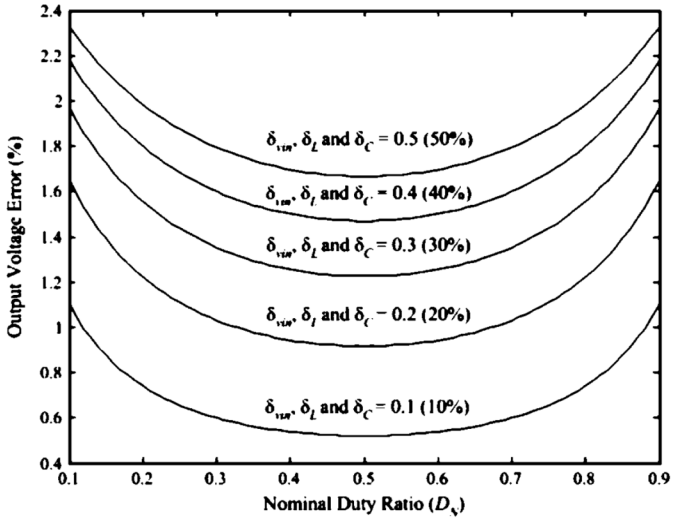

Fig. 9. Output voltage error versus duty ratio with different percentages of parametric variations.

III. Comparisons Among $\sigma*, \sigma^1, \sigma^2$, and σ^N

By expanding the logarithmic function in (16) with the Taylor series

$$\sigma^N|_{N\to\infty} = R\left[i_C + c_1\left[\sum_{n=1}^{N} -\frac{1}{n}\left(\frac{i_C}{c_1}\right)^n\right]\right] + (v_C - v_{\rm ref}) \quad (17)$$

and putting $N = 0$, 1, 2, respectively, it can be shown that

$$\sigma^N|_{N=0} = Ri_C + (v_C - v_{\rm ref}) \quad (18)$$

$$\sigma^N|_{N=1} = v_C - v_{\rm ref} \quad (19)$$

$$\sigma^N|_{N=2} = -\frac{R}{2}\frac{i_C^2}{c_1} + (v_C - v_{\rm ref}). \quad (20)$$

Equation (18) gives the typical mathematical expression of the switching surface for the sliding-mode control. Equation (19) gives the typical expression switching surface for the hysteresis control. By substituting the values of k_1 in (5) and k_2 in (11) for c_1 in (20), it can be shown that

$$\sigma^N|_{N=2} = \frac{Li_C^2}{2C(v_{\rm in} + \frac{v_C + v_{\rm ref}}{2})} + (v_C - v_{\rm ref}) \quad (21)$$

for switching S_1 and S_4 on and S_2 and S_3 off, and

$$\sigma^N|_{N=2} = -\frac{Li_C^2}{2C\left(v_{\rm in} - \frac{v_C + v_{\rm ref}}{2}\right)} + (v_C - v_{\rm ref}) \quad (22)$$

for switching S_2 and S_3 on and S_1 and S_4 off.

Equations (21) and (22) give similar expressions as the switching surface σ^2 proposed in [23], [26], and [27]. Thus, σ^2 is also the low-order approximation of σ^N.

In the following analysis, a pure mathematical treatment on comparing the discrepancies of σ^1, σ^2, and σ^N with σ^* is conducted. All switching surfaces are considered as continuous mathematical functions. No intracycle switching behaviors are taken into account. For the sake of comparison the values of v_C and i_C along the respective switching surface are normalized by the values at the operating point. The switching surfaces are compared by studying those surfaces on a $\hat{i}_C$-$\hat{v}_C$ plane, where $\hat{i}_C$ and $\hat{v}_C$ are the normalized values of i_C and v_C, respectively, v_C is normalized by the base value of $v_{\rm ref}$. That is

$$\hat{v}_C = \frac{v_C}{v_{\rm ref}} \quad (23)$$

i_C is normalized by the base value of $i_{C,n}$,

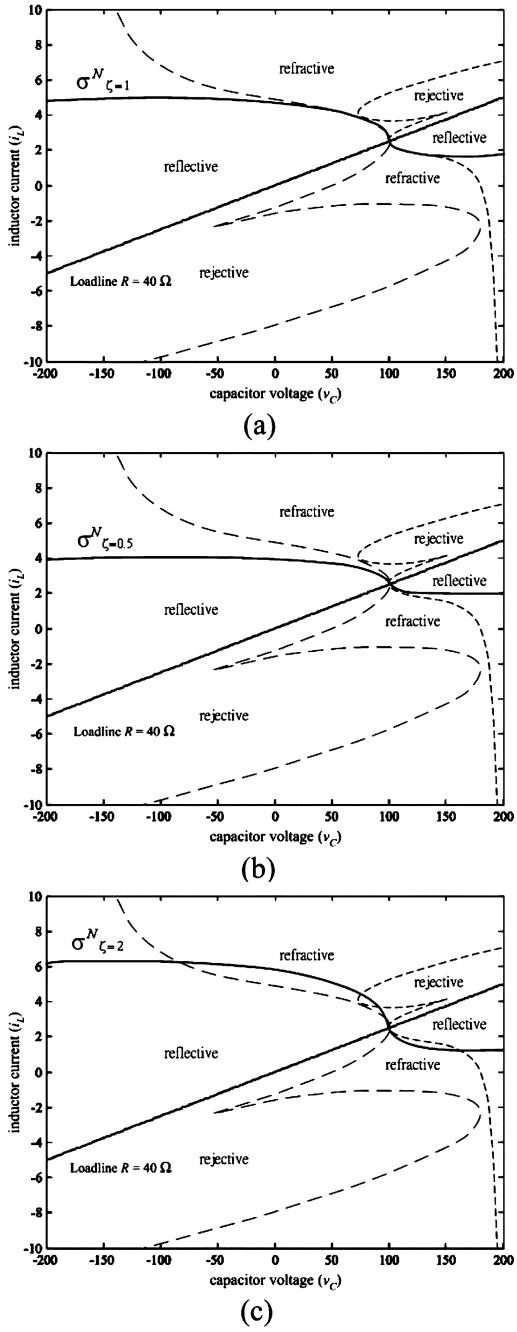

Fig. 10. Illustration of the switching surfaces and switching boundaries. (a) k_1 and k_2 are ideal ($\zeta_{S_{1,4}} = \zeta_{S_{2,3}} = 1$). (b) k_1 and k_2 are one half of the ideal values ($\zeta_{S_{1,4}} = \zeta_{S_{2,3}} = 0.5$). (c) k_1 and k_2 are twice the ideal values ($\zeta_{S_{1,4}} = \zeta_{S_{2,3}} = 2$).

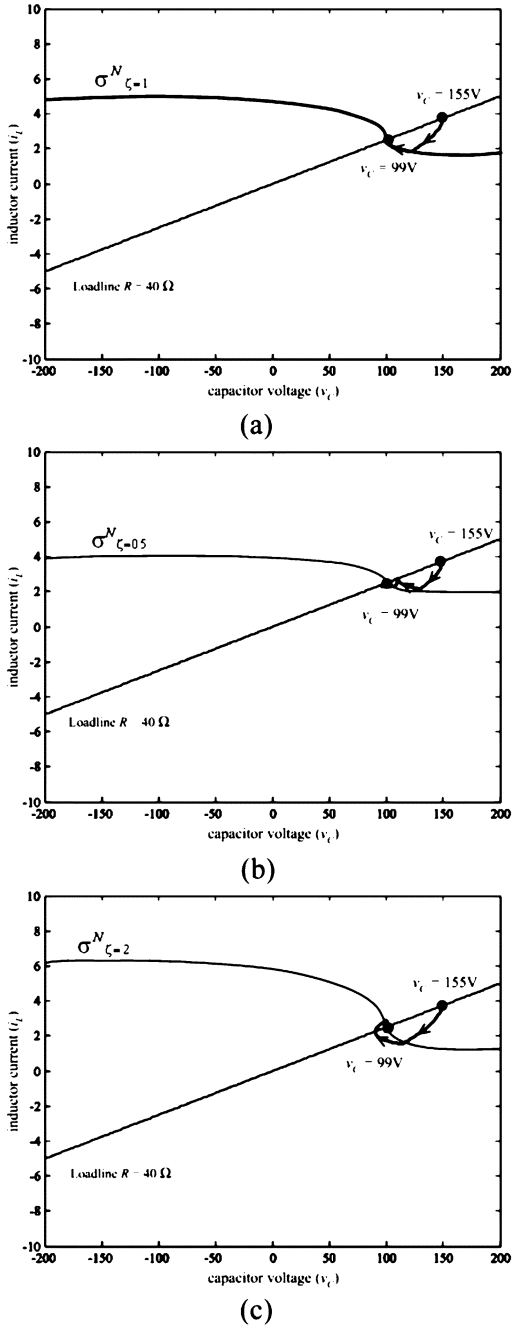

Fig. 11. Simulated state-space trajectories of the inverter various k_1 and k_2 with the switching boundaries. (a) k_1 and k_2 are ideal ($\zeta_{S_{1,4}} = \zeta_{S_{2,3}} = 1$). (b) k_1 and k_2 are one half of the ideal values ($\zeta_{S_{1,4}} = \zeta_{S_{2,3}} = 0.5$). (c) k_1 and k_2 are twice the ideal values ($\zeta_{S_{1,4}} = \zeta_{S_{2,3}} = 2$).

which is equal to

$$i_{C,n} = \frac{v_{\text{ref}}}{Z_C} \tag{24}$$

where $Z_C = (1/2)\sqrt{(L/C)}$ is the load impedance that the output filter is in critical damping. Detailed derivation of Z_C is given in the Appendix.

Thus

$$\hat{i}_C = \frac{i_C}{i_{C,n}}. \tag{25}$$

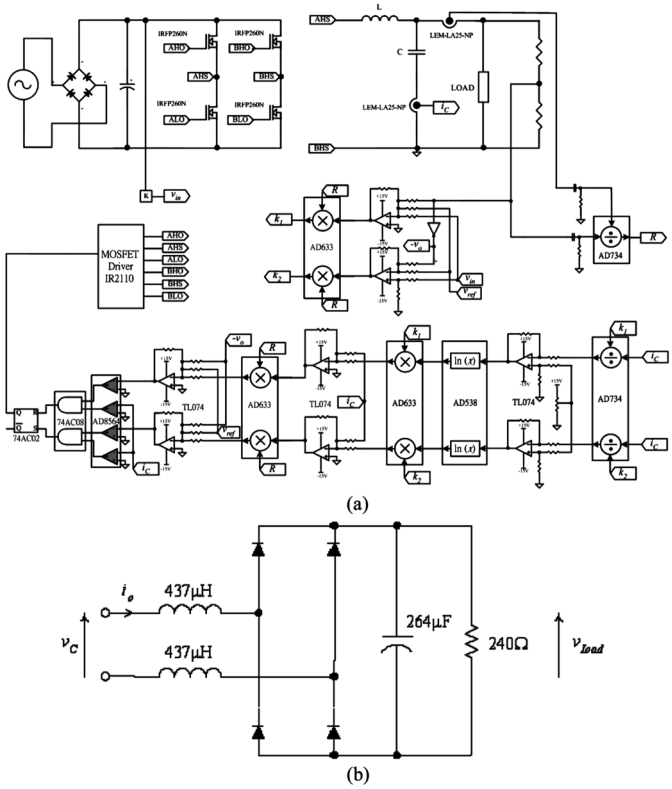

Fig. 12. Hardware implementation. (a) Schematic of the prototype. (b) Schematic of the full-wave rectifier load.

By putting (23) and (25) into (16), (18), and (20), the normalized switching surfaces $\hat{\sigma}^N, \hat{\sigma}^1$, and $\hat{\sigma}^2$ of σ^N, σ^1, and σ^2, respectively, with different load resistances are equal to

$$\hat{\sigma}^1 = R\hat{i}_C + Z_C\hat{v}_C - Z_C \tag{26}$$

$$\hat{\sigma}^2 = c_1\hat{i}_C^2 + \frac{Z_C^2}{v_{\text{ref}}}\hat{v}_C - \frac{Z_C^2}{v_{\text{ref}}} \tag{27}$$

$$\hat{\sigma}^N = R\left[\hat{i}_C + c_1\frac{Z_C}{v_{\text{ref}}}\ln\left(1 - \frac{v_{\text{ref}}}{Z_C}\frac{\hat{i}_C}{c_1}\right)\right] + (Z_C\hat{v}_C - Z_C). \tag{28}$$

When the inverter reaches the steady state, $v_C = v_{\text{ref}}$ and $i_C = 0$. Thus, the normalized operating point $(\hat{v}_{C,o}, \hat{i}_{C,o})$ on the $\hat{i}_C$-$\hat{v}_C$ plane is

$$\hat{v}_C = 1 \tag{29}$$

and

$$\hat{i}_C = 0. \tag{30}$$

The normalized ideal switching surface $\hat{\sigma}^*$ is obtained by putting (23) and (25) into (1). A comparison of $\hat{\sigma}^1, \hat{\sigma}^2, \hat{\sigma}^N$, and $\hat{\sigma}^*$ is shown in Fig. 5. Among them, $\hat{\sigma}^1$ deviates considerably from $\hat{\sigma}*, \hat{\sigma}^2$ gives closer approximation to $\hat{\sigma}*$ around the operating point, and $\hat{\sigma}^N$ gives the best approximation of $\hat{\sigma}*$ over the operating range.

Figs. 6 and 7 show the comparisons of the simulated time-domain waveforms, including v_C, i_L, and the gate signal to S_2 and S_3, v_g, and the state-space trajectories with various switching surfaces under a large-signal reference voltage change from the

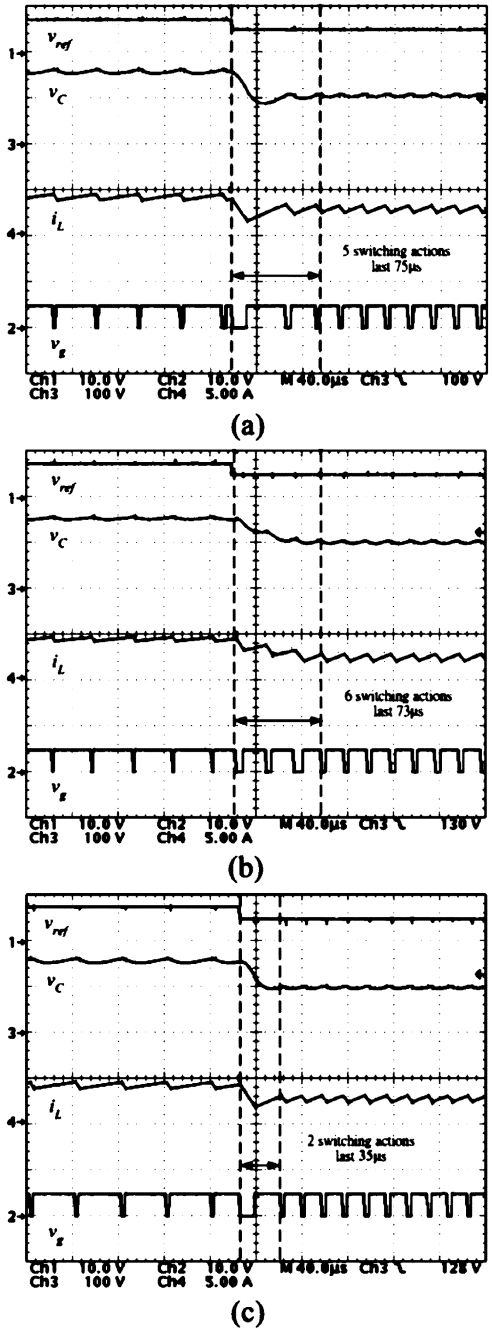

Fig. 13. Dynamic response of the inverter when the reference signal is changed from 110 $V_{\rm rms}$ to 70 $V_{\rm rms}$ at the angle around 90° [Ch1: $v_{\rm ref}$ (10 V/div), Ch2: v_g (10 V/div), Ch3: v_C (100 V/div), Ch4: i_L (5 A/div), timebase: 40 μs/div].

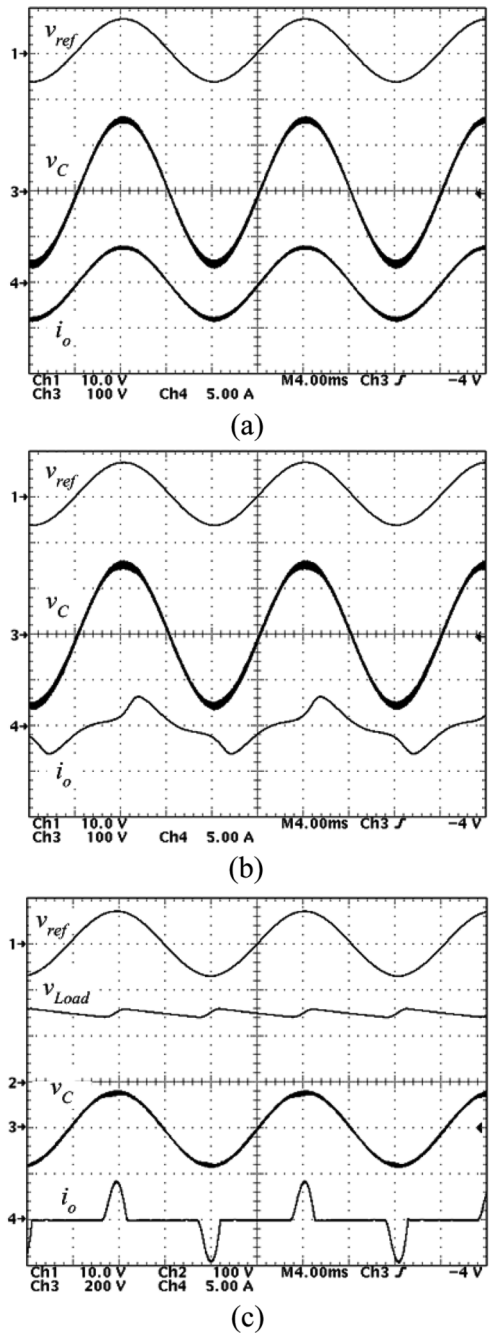

Fig. 14. Steady-state operations of the inverter [Ch1: $v_{\rm ref}$ (10 V/div), Ch2: $v_{\rm Load}$ (100 V/div), Ch3: v_C (100 V/div), Ch4: i_o (5 A/div), timebase: 4 ms/div]. (a) Resistive load. (b) Nonlinear inductive load. (c) Full-wave rectifier load.

peak voltage of 70 $V_{\rm rms}$ (i.e., 99 V) to 110 $V_{\rm rms}$ (i.e., 155 V) and vice versa. The parameters used are given in Table I. The settling times of the system with different switching surfaces are given in Table III. It can be observed that the one with σ^N gives the shortest settling time, confirming the advantages of the proposed control.

IV. Steady-State Characteristics

As described in Section III, σ^2 is the low-order approximation of σ^N. The inverter gives similar steady-state characteristics around the operating point with the two switching surfaces. Thus, in order to simplify the analysis, the steady-state characteristics of the inverter with σ^N, including the average output voltage $v_{\rm avg}$, output ripple voltage $v_{\rm ripple}$, and switching frequency f_s, are studied by applying the formulas in [26] for σ^2. Based on the equations derived in [26], $v_{\rm avg}, v_{\rm ripple}$, and f_s can be expressed as

$$v_{\rm avg} = v_{\rm ref} + \frac{\frac{L}{2C(v_{\rm in}+v_{\rm ref})} - \frac{L}{2C(v_{\rm in}-v_{\rm ref})} - (\beta_1 - \beta_2)}{\beta_1 + \beta_2}$$
$$\Delta_N = v_{\rm ref} \tag{31}$$

$$v_{\text{ripple}} = \frac{2Lv_{\text{in}}\Delta_N}{C(\beta_1+\beta_2)(v_{\text{in}}+v_{\text{ref}})(v_{\text{in}}-v_{\text{ref}})} \tag{32}$$

$$f_s = \frac{(v_{\text{in}}+v_{\text{ref}})(v_{\text{in}}-v_{\text{ref}})}{2Lv_{\text{in}}\left(\sqrt{\frac{\Delta_N}{\beta_1}}+\sqrt{\frac{\Delta_N}{\beta_2}}\right)} \tag{33}$$

where

$$\beta_1 = (L)/(2C(v_{\text{in}}+v_{\text{ref}})), \beta_2 = (L)/(2C(v_{\text{in}}-v_{\text{ref}})),$$

and Δ_N is the hysteresis band.

Based on (31), the average output voltage is the same as the reference voltage.

Equation (33) can also be rewritten as

$$f_s = \frac{1}{\alpha}d(1-d) \tag{34}$$

where

$$d = (1/2)(1+(v_{\text{ref}})/(v_{\text{in}}))$$

and

$$\alpha = (L)/(2v_{\text{in}})(\sqrt{(\Delta_N)/(\beta_1)}+\sqrt{(\Delta_N)/(\beta_2)}).$$

By differentiating (34) with respect to v_{ref}, it can be shown that

$$\frac{df_s}{dv_{\text{ref}}} = \frac{1}{\alpha}(1-2d). \tag{35}$$

Thus, f_s is maximum, when $d = 0.5$ and $v_{\text{ref}} = 0$. Fig. 8 shows the relationships between f_s and v_{ref} (and d). They are in a parabolic function. The relationships between f_s and v_{ref} are illustrated with five operating points marked with "1" to "5." It should be noted that f_s is much higher than the inverter output frequency.

V. Effects of the Parametric Variations on the Average Output Voltage

As the switching surface parameters k_1 in (5) and k_2 in (11) are dependent on the values of L and C. σ^N becomes non-ideal if there is a parametric variation in the values of L and C. Assume that

$$v_{\text{in}} = v_{\text{in},N}(1+\delta_{v_{\text{in}}}) \tag{36}$$

$$L = L_N(1+\delta_L) \tag{37}$$

$$C = C_N(1+\delta_C) \tag{38}$$

where $v_{\text{in},N}, L_N$, and C_N are the nominal values of v_{in}, L and C, respectively, $\delta_{v_{\text{in}}}, \delta_L$, and δ_C are the fractional changes in v_{in}, L, and C, respectively.

By substituting (36)–(38) into (31), it can be shown that the maximum output voltage error is equal to

$$\Delta v_{\text{avg}} = \left(\left(\frac{2D_N-1}{2D_N(1-D_N)}\right)\delta_{v_{\text{in}}} - \frac{2D_N-1}{D_N}\delta_L + \frac{2D_N-1}{D_N}\delta_C + \cdots\right)\Delta_N \tag{39}$$

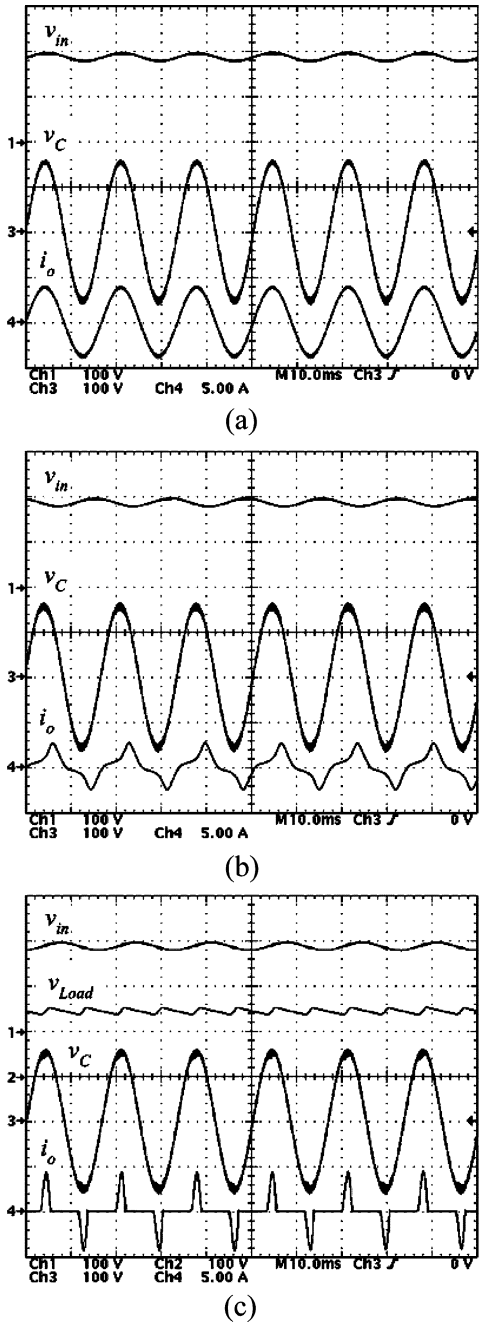

Fig. 15. Steady-state operation with 10% input voltage variation [Ch1: v_{in} (100 V/div), Ch2: v_{Load} (100 V/div), Ch3: v_C (100 V/div), Ch4: i_o (5 A/div), timebase: 10 ms/div]. (a) Resistive load. (b) Nonlinear inductive load. (c) Full-wave rectifier load.

where $D_N = (1/2)(1+(v_{\text{ref}})/(v_{\text{in},N}))$ is nominal duty cycle.

Thus, the output voltage drift has the same sensitivity to the variations in L and C. The sensitivity is the lowest when D_N equals 0.5 and the sensitivity is the highest when D_N equals 0 or 1. The steady-state output voltage error against the input voltage variation is minimum when $D_N = 0.5$. Fig. 9 shows the output voltage error versus D_N at different percentages of parametric variations. With 50% variation in the three parameters, the output voltage has a maximum error of 2.33% at $D_N = 0.1$ and 0.9.

VI. Large-Signal Characteristics

Points along $\sigma^N = 0$ in (16) can be classified into refractive, reflective, and rejective modes. The dynamics of the system behaves differently in those regions [18] and is studied by observing the correlation between the transition boundary and the switching surface. Basically, the value of c_1 in (16) determines the dynamic characteristics. Assume that c_1 is a factor of the ideal value of k_1, as defined in (5), when S_1 and are on. That is

$$c_1 = \zeta_{S_{1,4}} k_1 \tag{40}$$

where $\zeta_{S_{1,4}}$ is the discrepancy factor. If $\zeta_{S_{1,4}} = 1$, the inverter follows the derived switching surface. As there are discrepancies between the ideal component values and the actual component values, $\zeta_{S_{1,4}} \neq 1$, resulting in behaving non-ideal dynamic response.

The transition boundary with S_1 and on is obtained by differentiating (16) that $(di_L)/(dv_C)|_{S_{1,4}}$ in (41), shown at the bottom of the page, is obtained by using (1). Thus, equation (41) becomes (42), shown at the bottom of the page.

Similarly, the transition boundary with and S_3 on is obtained by differentiating (16) that

$$c_1 = \zeta_{S_{2,3}} k_2 \tag{43}$$

where $\zeta_{S_{2,3}}$ is the discrepancy factor between c_1 and the ideal value of k_2, as defined in (11). If $\zeta_{S_{2,3}} = 1$, the inverter follows the derived switching surface as (44), shown at the bottom of the page, where $(di_L)/(dv_C)|_{S_{2,3}}$ is also obtained by using (1). Thus, (44) becomes (45), shown at the bottom of the page. Detailed derivations of (42) and (45) are given in Appendix I.

As shown in Fig. 10(a), if the values of $\zeta_{S_{1,4}} = \zeta_{S_{2,3}} = 1$, the switching surface lies along the transition boundaries and is between the reflective and refractive regions when it is close to the operating point. This leads to good dynamic response to disturbances that the converter will settle to the steady state in two switching actions. However, the switching surface starts deviating from the transition boundaries, when the state point

$$R\left[\begin{array}{l} i_L - \frac{v_C}{R} + \left(R\frac{\left(i_L-\frac{v_C}{R}\right)\left(v_{\rm in}+\frac{v_C+v_{\rm ref}}{2}\right)}{v_{\rm in}+v_{\rm ref}} \left.\frac{di_L}{dv_C}\right|_{S_{1,4}} - \frac{R}{2}\frac{\left(i_L-\frac{v_C}{R}\right)\left(i_L-\frac{v_{\rm ref}}{R}\right)}{(v_{\rm in}+v_{\rm ref})} \right) \\ \cdot \ln\left(1 - \frac{i_L-\frac{v_C}{R}}{\left(R\frac{\left(i_L-\frac{v_C}{R}\right)\left(v_{\rm in}+\frac{v_C+v_{\rm ref}}{2}\right)}{v_{\rm in}+v_{\rm ref}} \left.\frac{di_L}{dv_C}\right|_{S_{1,4}} - \frac{R}{2}\frac{\left(i_L-\frac{v_C}{R}\right)\left(i_L-\frac{v_{\rm ref}}{R}\right)}{(v_{\rm in}+v_{\rm ref})} \right)} \right) \end{array}\right] + (v_C - v_{\rm ref}) = 0 \tag{41}$$

$$R\left[\begin{array}{l} i_L - \frac{v_C}{R} - \left(\frac{CR}{L}\frac{v_{\rm in}+v_C}{v_{\rm in}+v_{\rm ref}}\left(v_{\rm in}+\frac{v_C+v_{\rm ref}}{2}\right) + \frac{R}{2}\frac{\left(i_L-\frac{v_C}{R}\right)\left(i_L-\frac{v_{\rm ref}}{R}\right)}{(v_{\rm in}+v_{\rm ref})} \right) \\ \cdot \ln\left(1 + \frac{i_L-\frac{v_C}{R}}{\left(\frac{CR}{L}\frac{v_{\rm in}+v_C}{v_{\rm in}+v_{\rm ref}}\left(v_{\rm in}+\frac{v_C+v_{\rm ref}}{2}\right) + \frac{R}{2}\frac{\left(i_L-\frac{v_C}{R}\right)\left(i_L-\frac{v_{\rm ref}}{R}\right)}{(v_{\rm in}+v_{\rm ref})} \right)} \right) \end{array}\right] + (v_C - v_{\rm ref}) = 0 \tag{42}$$

$$R\left[\begin{array}{l} i_L - \frac{v_C}{R} + \left(R\frac{\left(i_L-\frac{v_C}{R}\right)\left(v_{\rm in}-\frac{v_C+v_{\rm ref}}{2}\right)}{v_{\rm in}-v_{\rm ref}} \left.\frac{di_L}{dv_C}\right|_{S_{2,3}} + \frac{R}{2}\frac{\left(i_L-\frac{v_C}{R}\right)\left(i_L-\frac{v_{\rm ref}}{R}\right)}{(v_{\rm in}-v_{\rm ref})} \right) \\ \cdot \ln\left(1 - \frac{i_L-\frac{v_C}{R}}{\left(R\frac{\left(i_L-\frac{v_C}{R}\right)\left(v_{\rm in}-\frac{v_C+v_{\rm ref}}{2}\right)}{v_{\rm in}-v_{\rm ref}} \left.\frac{di_L}{dv_C}\right|_{S_{2,3}} + \frac{R}{2}\frac{\left(i_L-\frac{v_C}{R}\right)\left(i_L-\frac{v_{\rm ref}}{R}\right)}{(v_{\rm in}-v_{\rm ref})} \right)} \right) \end{array}\right] + (v_C - v_{\rm ref}) = 0 \tag{44}$$

$$R\left[\begin{array}{l} i_L - \frac{v_C}{R} + \left(\frac{CR}{L}\frac{v_{\rm in}-v_C}{v_{\rm in}-v_{\rm ref}}\left(v_{\rm in}-\frac{v_C+v_{\rm ref}}{2}\right) + \frac{R}{2}\frac{\left(i_L-\frac{v_C}{R}\right)\left(i_L-\frac{v_{\rm ref}}{R}\right)}{(v_{\rm in}-v_{\rm ref})} \right) \\ \cdot \ln\left(1 - \frac{i_L-\frac{v_C}{R}}{\left(\frac{CR}{L}\frac{v_{\rm in}-v_C}{v_{\rm in}-v_{\rm ref}}\left(v_{\rm in}-\frac{v_C+v_{\rm ref}}{2}\right) + \frac{R}{2}\frac{\left(i_L-\frac{v_C}{R}\right)\left(i_L-\frac{v_{\rm ref}}{R}\right)}{(v_{\rm in}-v_{\rm ref})} \right)} \right) \end{array}\right] + (v_C - v_{\rm ref}) = 0 \tag{45}$$

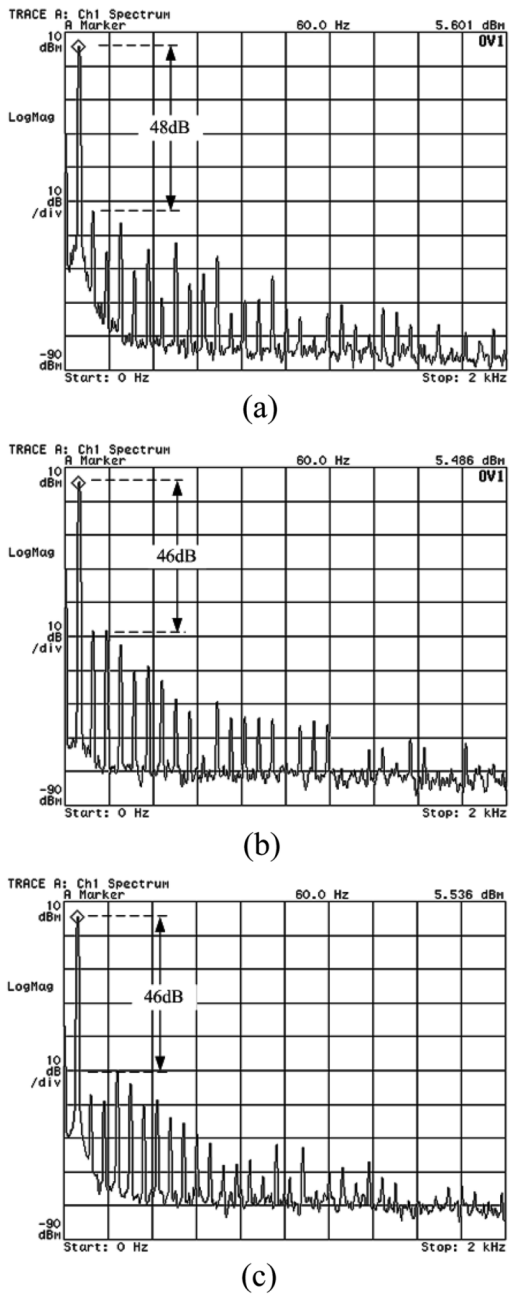

Fig. 16. Harmonic spectra of the output voltage. (a) Resistive load. (b) Nonlinear inductive load. (c) Full-wave rectifier load.

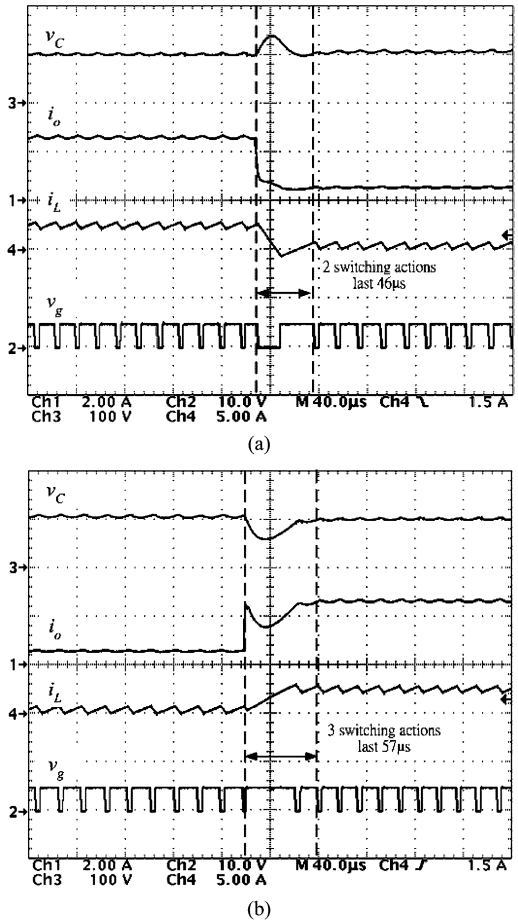

Fig. 17. Transient responses under load changes. (a) Rated load to 20% load. (b) 20% load to rated load. [Ch1: i_o (2 A/div), Ch2: v_g (10 V/div), Ch3: v_C (100 V/div), Ch4: i_L (5 A/div), timebase: 40 μs/div].

is far from the operating point. This is consistent with the comparison of σ^* and σ^N shown in Fig. 5. The inverter will then require more switching cycles to settle under a large-signal disturbance.

Fig. 10(b) shows the transition boundaries and the switching surface with $\zeta_{S_{1,4}} = \zeta_{S_{2,3}} = 0.5$. The switching surface almost lies on the reflective region. The implication is that the inverter is operating in sliding mode when it is subject to external disturbance.

Fig. 10(c) shows the transition boundaries and the switching surface with $\zeta_{S_{1,4}} = \zeta_{S_{2,3}} = 2$. The whole switching surface almost lies on the refractive region. The implication is that the inverter's trajectory will move toward the operating point in a spiral manner.

With $\zeta_{S_{1,4}}$ and/or $\zeta_{S_{2,3}}$ not equal to unity, the inverter will requires more switching actions before getting into the steady-state operating point. Fig. 11 shows the transient responses of the converter with different values of $\zeta_{S_{1,4}}$ and $\zeta_{S_{2,3}}$. The dynamic behaviors are the best when $\zeta_{S_{1,4}} = \zeta_{S_{2,3}} = 1$.

VII. Experimental Verifications

A 300 W, 110 V, 60 Hz full bridge inverter has been built and tested. The schematic of the circuit is shown in Fig. 12(a). The component values are tabulated in Table I. As shown in Appendix I, the filter is designed to make it operate at the critical damping condition and rated power condition. As the power rating is 300 W and the voltage rating is 110 V, $Z = 40\ \Omega$. The cutoff frequency f_C of the filter, which is chosen to be one-fourth of the minimum switching frequency of 25 kHz, equals 6.3 kHz. By putting Z and $\omega_n = 2\pi f_C$ into (A1) and (A2), the values of L and C shown in Table I are calculated.

Fig. 13 shows the enlarged waveforms of the dynamic responses of the inverter supplying to the 40 Ω resistive load with different switching surfaces, including σ^N, σ^2 and σ^1. The reference voltage is suddenly changed at the peak of the reference signal from 70 $V_{\rm rms}$ to 110 $V_{\rm rms}$. The transient periods of the

inverters with σ^1, σ^2, and σ^N are 75 μs, 73 μs, and 35 μs, respectively. Among them, σ^N gives the best dynamic response. As shown in Fig. 13(c), the inverter only takes two switching actions getting into the steady state. The output voltage looks constant before and after the disturbance, because the timebase of measurement is 40 μs and is much shorter than the period of the output voltage, which is 1/60 Hz = 16.67 ms. The variation of the output voltage is thus very small.

Fig. 14 shows the steady-state output voltage waveforms supplying to resistive, nonlinear inductive, and full-wave rectifier loads. The output voltage is sinusoidal in all cases. The load specifications are tabulated in Table II. The schematic of the full-wave rectifier load is shown in Fig. 12(b). Fig. 15 shows the steady-state waveforms when the dc input voltage has fluctuation of 10%. The purpose is to simulate the condition that the dc rail is derived by rectifying the ac voltage shown in Fig. 12(a) and the proposed method can still provide a sinusoidal waveform with low total harmonic distortion (THD). It should be noted here that similar steady-state waveforms can be obtained with σ^1 and σ^2, because all three switching surfaces are close to $\sigma*$ around the operating point (Section III). However, σ^N gives better large-signal dynamic responses.

Fig. 16 shows the harmonic spectra of the output voltage with different loads. The third harmonics (180 Hz) is less than the fundamental component (60 Hz) by more than 45 dB in both cases. The THD of the output voltage is less than 1.1%. Fig. 17 shows the transient responses of the output voltage when the resistive load is changed from the rated load to 20% load, and vice versa. The inverter can revert to the steady state in two to three switching actions. As explained in Section VI, the required switching action is more than two if the inverter state point is far from the steady-state operating point. Nevertheless, the inverter output voltage can still get into the 3% band within two switching actions. Thus, apart from providing fast dynamic response, the proposed control method can equally give good output harmonic spectra in inverter applications.

VIII. Conclusion

A high-order switching surface σ^N for boundary control of inverters has been presented. Some concluding remarks are listed as follows.

1) The generalized form of σ^N has been given in (16).
2) The first- and second-order switching surfaces have been shown to be the low-order approximation of σ^N in (26)–(28).
3) The steady-state characteristics, including the average output voltage, output ripple voltage, and switching frequency, have been given in (31)–(35).
4) The effects of the parametric variations on the average output voltage have been studied in (39).
5) The large-signal characteristics of the control method have been studied in Section VI.

Moreover, the control method does not require any sophisticated calculations of the transfer functions or closed-loop compensation. The controller's parameters are obtained readily by considering the component values of the power stage. It is unnecessary to determine the controller parameters by the trail-and-error approach. Most importantly, the control method is for large-signal control. The proposed method has been confirmed experimentally. Further research will be dedicated into the boundary control with constant switching frequency.

Appendix

A. Derivation of Z_C in (24)

As shown in [28], the transfer function $G(s)$ of the output filter is a second-order system. It can be shown that

$$G(s) = \frac{v_C(s)}{v_x(s)} = \frac{\omega_n^2}{s^2 + 2\xi\omega_n s + \omega_n^2} \tag{A1}$$

where $\omega_n = \sqrt{(1)/(LC)}$ and $\xi = (1)/(2CZ\omega_n)$ are the natural frequency and damping ratio of the filter, respectively.

The filter will be in critical damping (i.e., $\xi = 1$) when

$$Z = Z_C = \frac{1}{2}\sqrt{\frac{L}{C}}. \tag{A2}$$

B. Derivations of (41), (42), (44), and (45)

Substitute $c_1 = \zeta_{S_{1,4}} k_1 = \zeta_{S_{1,4}}(CR)/(L)(-v_{\text{in}} - (v_C + v_{\text{ref}})/(2))$ into (16) with $\sigma^N = 0$

$$R\left[\begin{array}{l} i_C + \zeta_{S_{1,4}}\frac{CR}{L}\left(-v_{\text{in}} - \frac{v_C+v_{\text{ref}}}{2}\right) \\ \cdot \ln\left(1 - \frac{i_C}{\zeta_{S_{1,4}}\frac{CR}{L}\left(-v_{\text{in}} - \frac{v_C+v_{\text{ref}}}{2}\right)}\right)\end{array}\right] + (v_C - v_{\text{ref}}) = 0. \tag{A3}$$

Then, by differentiating both sides of (A3), it gives

$$\zeta_{S_{1,4}} = -\frac{L}{C}\frac{i_L - \frac{v_C}{R}}{v_{\text{in}} + v_{\text{ref}}}\left.\frac{di_L}{dv_C}\right|_{S_{1,4}} + \frac{L}{2C}\frac{\left(i_L - \frac{v_C}{R}\right)\left(i_L - \frac{v_{\text{ref}}}{R}\right)}{\left(v_{\text{in}} + \frac{v_C+v_{\text{ref}}}{2}\right)(v_{\text{in}} + v_{\text{ref}})}. \tag{A4}$$

Equation (41) can then be derived by substituting the value of (A4) into (A3). Similarly, substitute $c_1 = \zeta_{S_{2,3}} k_2 = \zeta_{S_{2,3}}(CR)/(L)(v_{\text{in}} - (v_C + v_{\text{ref}})/(2))$ into (16) with $\sigma^N = 0$

$$R\left[\begin{array}{l} i_C + \zeta_{S_{2,3}}\frac{CR}{L}\left(v_{\text{in}} - \frac{v_C+v_{\text{ref}}}{2}\right) \\ \cdot \ln\left(1 - \frac{i_C}{\zeta_{S_{2,3}}\frac{CR}{L}\left(v_{\text{in}} - \frac{v_C+v_{\text{ref}}}{2}\right)}\right)\end{array}\right] + (v_C - v_{\text{ref}}) = 0. \tag{A5}$$

Again, by differentiating both sides of (A5)

$$\zeta_{S_{2,3}} = \frac{L}{C}\frac{i_L - \frac{v_C}{R}}{v_{\text{in}} - v_{\text{ref}}}\left.\frac{di_L}{dv_C}\right|_{S_{2,3}} + \frac{L}{2C}\frac{\left(i_L - \frac{v_C}{R}\right)\left(i_L - \frac{v_{\text{ref}}}{R}\right)}{\left(v_{\text{in}} - \frac{v_C+v_{\text{ref}}}{2}\right)(v_{\text{in}} - v_{\text{ref}})}. \tag{A6}$$

Equation (44) can then be derived by substituting the value of (A6) into (A5). Based on (1)

$$\left.\frac{di_L}{dv_C}\right|_{S_{1,4}} = -\frac{C}{L}\frac{v_{\text{in}} + v_C}{i_L - \frac{v_C}{R}} \tag{A7}$$

$$\left.\frac{di_L}{dv_C}\right|_{S_{2,3}} = \frac{C}{L}\frac{v_{\text{in}} - v_C}{i_L - \frac{v_C}{R}}. \tag{A8}$$

By putting (A7) and (A8) into (41) and (44), respectively, (42) and (45) can be obtained.

REFERENCES

[1] K. Taniguchi, Y. Ogino, and H. Irie, "PWM technique for power MOSFET inverter," *IEEE Trans. Power Electron.*, vol. PE-3, no. 3, pp. 328–334, Jul. 1988.

[2] J. Holtz, "Pulsewidth modulation for electronic power conversion," *Proc. IEEE*, vol. 82, no. 8, pp. 1194–1214, Aug. 1994.

[3] J. W. Kolar, H. Ertl, and F. C. Zach, "Influence of the modulation method on the conduction and switching losses of a PWM converter system," *IEEE Trans. Ind. Appl.*, vol. 27, no. 6, pp. 1063–1075, Nov./Dec. 1991.

[4] H. Kim, H. Lee, and S. Sul, "A new PWM strategy for common-mode voltage reduction in neutral-point-clamped inverter-fed AC motor drives," *IEEE Trans. Ind. Appl.*, vol. 37, no. 6, pp. 1840–1845, Nov./Dec. 2001.

[5] M. Kojima, K. Hirabayashi, Y. Kawabata, E. C. Ejiogu, and T. Kawabata, "Novel vector control system using deadbeat-controlled PWM inverter with output *LC* filter," *IEEE Trans. Ind. Appl.*, vol. 40, no. 1, pp. 162–169, Jan./Feb. 2004.

[6] K. Zhang, Y. Kang, J. Xiong, and J. Chen, "Direct repetitive control of SPWM inverter for UPS purpose," *IEEE Trans. Power Electron.*, vol. 18, no. 3, pp. 784–792, May 2003.

[7] O. Kukrer, H. Komurcugil, and N. S. Bayindir, "Control strategy for single-phase UPS inverter," *Proc. Inst. Elect. Eng.*, vol. 150, no. 6, pp. 743–746, Nov. 2003.

[8] S. R. Bowes, D. Holliday, and S. Grewal, "Regular-sampled harmonic elimination PWM control of single-phase two-level inverters," *Proc. Inst. Elect. Eng.*, vol. 148, no. 4, pp. 309–314, Jul. 2001.

[9] N. Hur, J. Jung, and K. Nam, "A fast dynamic dc-link power-balancing scheme for a PWM converter-inverter system," *IEEE Trans. Ind. Electron.*, vol. 48, no. 4, pp. 794–803, Aug. 2001.

[10] J. C. Liao and S. N. Yeh, "A novel instantaneous power control strategy and analytic model for integrated rectifier/inverter systems," *IEEE Trans. Power Electron.*, vol. 15, no. 6, pp. 996–1006, Nov. 2000.

[11] J. Holtz and B. Beyer, "Optimal synchronous pulsewidth modulation with a trajectory-tracking scheme for high-dynamic performance," *IEEE Trans. Ind. Appl.*, vol. 29, no. 6, pp. 1098–1105, Nov./Dec. 1993.

[12] R. Munzert and P. T. Krein, "Issues in boundary control," in *Proc. IEEE Power Electron. Spec. Conf.*, 1996, pp. 810–816.

[13] R. M. Bass and P. T. Krein, "Switching boundary geometry and the control of single-phase inverters," in *Proc. IEEE Ind. Appl. Soc. Annu. Meeting*, 1989, pp. 1052–1056.

[14] S. H. Jung, N. I. Kim, and G. H. Cho, "Class D audio power amplifier with fine hysteresis control," *IEEE Electron. Lett.*, vol. 38, no. 2, pp. 1302–1303, Oct. 2002.

[15] T. L. Tai and J. S. Chen, "UPS inverter design using discrete-time sliding-mode control scheme," *IEEE Trans. Ind. Electron.*, vol. 49, no. 1, pp. 67–75, Feb. 2002.

[16] H. Ma and S. Han, "Analysis and design of sliding mode control for AC signal power amplifier," in *Proc. IEEE Ind. Electron. Soc. Conf.*, Nov. 2004, vol. 2, pp. 1652–1657.

[17] E. Chang, T. Lian, J. Chen, and R. Lin, "A sliding-mode controller based on fuzzy logic for PWM inverters," in *Proc. IEEE Asia-Pacific Conf. Circuit Syst.*, Dec. 2004, vol. 2, pp. 965–968.

[18] M. Greuel, R. Muyshondt, and P. T. Krein, "Design approaches to boundary controllers," in *Proc. IEEE Power Electron. Spec. Conf.*, 1997, pp. 672–678.

[19] D. Biel, E. Fossas, F. Guinjoan, E. Alarcon, and A. Poveda, "Application of sliding-mode control to the design of a buck-based sinusoidal generator," *IEEE Trans. Power Electron.*, vol. 48, no. 3, pp. 563–571, Jun. 2001.

[20] R. R. Ramos, D. Biel, E. Fossas, and F. Guinjoan, "A fixed-frequency quasi-sliding control algorithm: Application to power inverters design by means of FPGA implementation," *IEEE Trans. Power Electron.*, vol. 18, no. 1, pp. 344–355, Jan. 2003.

[21] W. M. P. Filho and A. J. Perin, "An approach of the variable structure analysis for power electronics applications," in *Proc. IEEE Ind. Appl. Soc. Annu. Meeting*, 1997, pp. 844–851.

[22] S. C. Tan, Y. M. Lai, C. K. Tse, and M. K. H. Cheung, "Adaptive feedforward and feedback control schemes for sliding mode controlled power converters," *IEEE Trans. Power Electron.*, vol. 21, no. 1, pp. 182–192, Jan. 2006.

[23] K. K. S. Leung and H. S. H. Chung, "Derivation of a second-order switching surface in the boundary control of buck converters," *IEEE Power Electron. Lett.*, vol. 2, no. 2, pp. 63–67, Jun. 2004.

[24] V. M. Nguyen and C. Q. Lee, "Tracking control of buck converter using sliding-mode with adaptive hysteresis," in *Proc. IEEE Power Electron. Spec. Conf.*, 1995, pp. 1086–1093.

[25] Y. He and F. L. Luo, "Design and analysis of adaptive sliding-mode-like controller for dc–dc converters," in *Proc. IEEE Electric Power Appl.*, Jan. 2006, vol. 153, no. 3, pp. 401–410.

[26] K. S. Leung and H. S. H. Chung, "A comparative study of the boundary control of buck converters using first- and second-order switching surfaces—Part I: Continuous conduction mode," in *Proc. IEEE Power Electron. Spec. Conf.*, 2005, pp. 2133–2139.

[27] K. K.-S. Leung and H. S. H. Chung, "A comparative study of boundary control with first- and second-order switching surfaces for Buck converters operating in DCM," *IEEE Trans. Power Electron.*, vol. 22, no. 4, pp. 1196–1209, Jul. 2007.

[28] M. Ordonez, M. T. Iqbal, and J. E. Quaicoe, "Selection of a curved switching surface for Buck converters," *IEEE Trans. Power Electron.*, vol. 21, no. 4, pp. 1148–1153, Jul. 2006.

Julian Yat-Chung Chiu (S'04) received the B.Eng. and M.Phil. degrees in electronic engineering from the City University of Hong Kong, Hong Kong, China, in 2002 and 2007, respectively.

He is currently a Research Assistant with the Department of Electronic Engineering, City University of Hong Kong. His research interests include dc–dc converters, dc–ac inverters, boundary control, digital audio systems, and maximum power point tracking of photovoltaic panel.

Kelvin Ka-Sing Leung (S'03–M'06) received the B.Eng. (with first class honors) and Ph.D. degrees in electronic engineering from the City University of Hong Kong, Hong Kong, China, in 2000 and 2005, respectively.

He is currently an Engineer in MKS Instruments, where he is working mainly in the area of dc and RF power generation. His research interests include dc–dc converter, switching surface control, and inverter applications.

Dr. Leung received the Chen Hsong Industrial Scholarships in 1999, the Chiap Hua Cheng's Foundation Scholarships, Shun Hing Education, and Charity Fund Scholarship, and the IEE Prize in 2000.

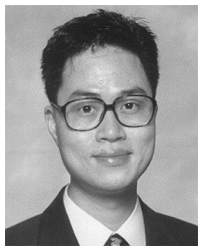

Henry Shu-Hung Chung (M'95–SM'03) received the B.Eng. and Ph.D. degrees in electrical engineering from the Hong Kong Polytechnic University, Hong Kong, China, in 1991 and 1994, respectively.

Since 1995, he has been with the City University of Hong Kong (CityU). He is currently Professor with the Department of Electronic Engineering and Chief Technical Officer of Energy Technology, Ltd. (an associated company of CityU). He has authored six research book chapters, and over 250 technical papers including 100 refereed journal papers in his research areas, and holds ten patents. His research interests include time- and frequency-domain analysis of power electronic circuits, switched-capacitor-based converters, random-switching techniques, control methods, digital audio amplifiers, soft-switching converters, and electronic ballast design.

Dr. Chung received the Grand Applied Research Excellence Award in 2001 from the City University of Hong Kong. He was Associate Editor and Guest Editor of the IEEE TRANSACTIONS ON CIRCUITS AND SYSTEMS—PART I: FUNDAMENTAL THEORY AND APPLICATIONS from 1999 to 2003. He is currently Associate Editor of the IEEE TRANSACTIONS ON POWER ELECTRONICS. He was IEEE Student Branch Counselor and was Track Chair of the Technical Committee on Power Electronics Circuits and Power Systems, IEEE Circuits and Systems Society, from 1997 to 1998.